

See discussions, stats, and author profiles for this publication at: <https://www.researchgate.net/publication/269282052>

Evolution of Lattice Structure and Chemical Composition of the Surface Reconstruction Layer in Li_{1.2}Ni_{0.2}Mn_{0.6}O₂ Cathode Material for Lithium Ion Batteries

ARTICLE *in* NANO LETTERS · DECEMBER 2014

Impact Factor: 13.59 · DOI: 10.1021/nl5038598 · Source: PubMed

CITATIONS

9

READS

127

16 AUTHORS, INCLUDING:



Anmin Nie

Michigan Technological University

37 PUBLICATIONS 253 CITATIONS

[SEE PROFILE](#)



Jianming Zheng

Pacific Northwest National Laboratory

61 PUBLICATIONS 1,479 CITATIONS

[SEE PROFILE](#)



Dongping Lv

Pacific Northwest National Laboratory

34 PUBLICATIONS 780 CITATIONS

[SEE PROFILE](#)



I. Belharouak

Qatar Environment and Energy Research Instit...

118 PUBLICATIONS 3,810 CITATIONS

[SEE PROFILE](#)

Evolution of Lattice Structure and Chemical Composition of the Surface Reconstruction Layer in $\text{Li}_{1.2}\text{Ni}_{0.2}\text{Mn}_{0.6}\text{O}_2$ Cathode Material for Lithium Ion Batteries

Pengfei Yan,[†] Anmin Nie,[‡] Jianming Zheng,[§] Yungang Zhou,^{||} Dongping Lu,[§] Xiaofeng Zhang,[⊥] Rui Xu,[⊥] Ilias Belharouak,^{⊥,¶} Xiaotao Zu,^{||} Jie Xiao,[§] Khalil Amine,[⊥] Jun Liu,[§] Fei Gao,[○] Reza Shahbazian-Yassar,[‡] Ji-Guang Zhang,^{*,§} and Chong-Min Wang^{*,†}

[†]Environmental Molecular Sciences Laboratory, Pacific Northwest National Laboratory, 902 Battelle Boulevard, Richland, Washington 99352, United States

[‡]Department of Mechanical Engineering-Engineering Mechanics, Michigan Technological University, 1400 Townsend Dr., Houghton, Michigan 49931, United States

[§]Energy and Environmental Directorate, Pacific Northwest National Laboratory, 902 Battelle Boulevard, Richland, Washington 99352, United States

^{||}Department of Applied Physics, University of Electronic Science and Technology of China, Chengdu 610054, People's Republic of China

[⊥]Chemical Sciences and Engineering Division, Argonne National Laboratory, 9700 South Cass Avenue, Argonne, Illinois 60439, United States

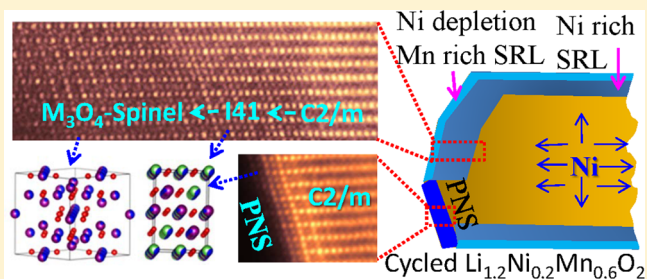
[¶]Qatar Environment and Energy Research Institute, Qatar Foundation, P.O. Box 5825, Doha, Qatar

[○]Department of Nuclear Engineering and Radiological Sciences, University of Michigan, Ann Arbor, Michigan 48109, United States

S Supporting Information

ABSTRACT: Voltage and capacity fading of layer structured lithium and manganese rich (LMR) transition metal oxide is directly related to the structural and composition evolution of the material during the cycling of the battery. However, understanding such evolution at atomic level remains elusive. On the basis of atomic level structural imaging, elemental mapping of the pristine and cycled samples, and density functional theory calculations, it is found that accompanying the hopping of Li ions is the simultaneous migration of Ni ions toward the surface from the bulk lattice, leading to the gradual depletion of Ni in the bulk lattice and thickening of a Ni enriched surface reconstruction layer (SRL). Furthermore, Ni and Mn also exhibit concentration partitions within the thin layer of SRL in the cycled samples where Ni is almost depleted at the very surface of the SRL, indicating the preferential dissolution of Ni ions in the electrolyte. Accompanying the elemental composition evolution, significant structural evolution is also observed and identified as a sequential phase transition of $C2/m \rightarrow I41 \rightarrow \text{Spinel}$. For the first time, it is found that the surface facet terminated with pure cation/anion is more stable than that with a mixture of cation and anion. These findings firmly established how the elemental species in the lattice of LMR cathode transfer from the bulk lattice to surface layer and further into the electrolyte, clarifying the long-standing confusion and debate on the structure and chemistry of the surface layer and their correlation with the voltage fading and capacity decaying of LMR cathode. Therefore, this work provides critical insights for design of cathode materials with both high capacity and voltage stability during cycling.

KEYWORDS: lithium ion battery, LMR cathode, surface reconstruction, ion migration, voltage fading, Ni surface segregation



Lithium-ion batteries (LIBs) have been commercialized for more than two decades. Nowadays, driven by the demand of portable electronic device market, the next generation LIBs, featured with high capacity, high operating voltage, and high rate capability, are under intense investigations.^{1–6} In general, the cathode materials play a key role in determining the performance of LIBs. Thus, exploring and developing advanced cathode materials attracts more and more efforts around

world.^{7–9} To date, Mn-based $\text{LiNi}_x\text{Mn}_{1-x-y}\text{Co}_y\text{O}_2$ (NCM), Ni-based $\text{LiNi}_{1-x-y}\text{Co}_x\text{Al}_y\text{O}_2$ (NCA), and Li–Mn-rich (LMR) cathode materials are among the most promising competitors in the cathode materials.^{1,10–16} However, commercialization of

Received: October 7, 2014

Revised: November 17, 2014

these cathode materials faces many challenges. For example, LMR cathode still suffered from voltage fading, capacity decay, cycling instability, and poor rate capability. Structurally, these three groups of cathode materials all exhibit a layered structure for pristine materials.^{17–20} After charge–discharge cycling, they all form a surface reconstruction layer (SRL),^{20–22} which have the following features: (1) formation of oxygen vacancies; (2) transition metal (TM) cations hopping into Li-sites; (3) TM cations being reduced to low valence state; and (4) lattice structure transformation. Obviously, the chemical and structural evolution of such a surface layer directly correlates to their electrochemical performance, which in essence has been attributed to one of the main causes for voltage fading, capacity decay, and cycling instability. In previous studies, several models have been proposed to interpret how the surface layer influences electrochemical performance of the cathode materials.^{21,23,24} Understanding of the structure, chemistry, and formation kinetics of the surface layer has been a hot topic in LIBs field and considerable efforts have been used to probe the nature of the surface layer by utilizing a variety of experimental and computational approaches.^{5,25–31}

Although the common features of SRL have been well recognized as mentioned above, it is still far from clear on the fundamental mechanism behind the formation and evolution SRL during the cycling process. It has been reported that TM cations will hop into Li-sites both in TM-slab and Li-slab in the SRL; however, the dynamics and the kinetic mechanism of TM cation migration are still unclear. There are also debates on which TM cation hops into Li-sites.^{5,18,21,31–33} The role of oxygen vacancies in promoting surface reconstruction also needs further study.^{3,26,34} Moreover, structural nature of the SRL is not clear, though rock salt,^{5,20,35} disordered rock salt,² and spinel (including disordered-spinel/spinel-like)^{10,21,23} structures have been used to describe the SRL structure. Compositionally, as compared with the bulk lattice, it is believed that the SRL is TM-rich and Li-poor,^{21,22} but quantitative description of the SRL is not established yet. Additionally, it has been identified that Ni is prone to segregate to certain surface facets of particle even for the pristine LMR cathode particles.^{28,36} The structure of such a pristine Ni-segregation surface (PNS) layer is very similar to the cycling induced SRL. However, detailed comparison between cycling induced SRL and PNS layer is lacking, which makes it hard to distinguish PNS and SRL.

In this work, using aberration-corrected scanning/transmission electron microscopes (S/TEM) equipped with high angle annular dark field/annular bright field (HAADF/ABF) detectors, advanced energy dispersive X-ray spectroscope (EDS) and electron energy loss spectroscope (EELS), we systematically studied the pristine and charge–discharge cycled $\text{Li}_{1.2}\text{Ni}_{0.2}\text{Mn}_{0.6}\text{O}_2$ (LMR) cathode materials prepared by coprecipitation method. Combining atomic level structural imaging, quantitative high spatial chemical analysis and computational simulation and calculation, we captured unprecedented details on the formation, structure, and composition of SRL. For the first time, we discovered that the formation of SRL layer is closely related to the hoping of Ni from TM layer to Li layer and subsequent migration of Ni from bulk lattice toward surface during the cyclic charge/discharge process, leading to the gradual depletion of Ni from the bulk lattice. The Ni and Mn ions at the very outer surface of the SRL show concentration partitions, with Ni almost being depleted at the very surface of the SRL, indicating preferential dissolution

of Ni ions in the electrolyte. Meanwhile, structural evolution is observed and identified as a sequential phase transition of $\text{C}2/m \rightarrow \text{I}41 \rightarrow$ spinel. The present work provides new insights as how structural and chemical evolutions of the SRL correlate with the voltage fading and capacity decaying of LMR cathode.

The LMR was synthesized by a coprecipitation process. Nickel sulfate hexahydrate ($\text{NiSO}_4 \cdot 6\text{H}_2\text{O}$), manganese sulfate monohydrate ($\text{MnSO}_4 \cdot \text{H}_2\text{O}$), sodium hydroxide (NaOH), and ammonium hydroxide ($\text{NH}_3 \cdot \text{H}_2\text{O}$) were used as the starting materials to prepare $\text{Ni}_{0.25}\text{Mn}_{0.75}(\text{OH})_2$ precursor. The precursor material was washed with deionized water to remove residual sodium and sulfuric species, followed by filtering and drying. Afterward, $\text{Ni}_{0.25}\text{Mn}_{0.75}(\text{OH})_2$ precursor was well mixed with Li_2CO_3 at a stoichiometric ratio for calcination (900 °C for 14 h) to get the final Li-excess cathode material. Coin cells were assembled with the as-prepared cathode materials, metallic lithium foil as counter electrode, Celgard K1640 monolayer polyethylene (PE) membrane as separator, and 1 M lithium hexafluorophosphate (LiPF_6) dissolved in ethyl carbonate (EC) and dimethyl carbonate (DMC) (1:2 in volume) as electrolyte in an argon-filled MBraun glovebox. Detailed experimental set up for cathode materials synthesis and electrochemical test can be found in our previous report.³⁷ The cathode samples were electrochemically tested by the following four methods: charged to 4.7 V (designated as 4.7 V sample); 5 cycles (5 cycled sample), 45 cycles (45 cycled sample) and 100 cycles (100 cycled sample). For the 4.7 V sample, the pristine sample was charged to 4.7 V at 0.1C rate. For the other three cells, they were cycled at a rate of 0.1C between 2.0 and 4.7 V vs Li/Li^+ at the room temperature.

Following the cycling of the battery, the obtained electrode was first immersed in DMC for 12 h and then washed by DMC for three times and dried in vacuum for 12h. The electrode were peeled off from the Al-foil and grounded to fine powders. The powder particles were dusted on a lacy carbon TEM grid for microanalysis. Two probe aberration-corrected S/TEM microscopes were used for the microstructural study: FEI Titan 80-300 and JEOL JEM-ARM200CF. The SAED, HRTEM, STEM-HAADF observations and EELS analysis were conducted using Titan 80-300 microscope operated at 300 kV. HAADF images was collected by the annular detector in the range of 55–220 mrad and EELS were acquired using Gatan Image Filter (GIF, Quantum 965) with collection semiangle ~50 mrad. The electron beam has a convergence angle of 17.8 mrad. The STEM-HAADF/ABF imaging and EDS mapping were performed on JEOL JEM-ARM200CF microscope operated at 200 kV with a Schottky cold-field emission gun. The HAADF and ABF pairs are simultaneously acquired with a beam convergence angle as 22 mrad. The HAADF and ABF images were acquired at 90–370 mrad and 11–22 mrad, respectively. The EDS elemental mapping was carried using the JEOL SDD-detector with a 100 mm^2 X-ray sensor, featuring a collection angle of ~10° of traditional detector and, therefore, enabling high sensitivity and high performance analysis. The EELS data were collected from thin area to reduce multiple inelastic scatterings. A low-loss spectrum and the core-loss spectrum were collected from the same area at the same time. The low-loss spectrum was used to remove the multiple inelastic scattering effect in the core-loss region using the Fourier ratio technique (DigitalMicrograph, Gatan Inc.).

Computer simulations of electron diffractions and HRTEM images were conducted by using JEMS software. For diffractions, sample thickness is 60 nm. For HRTEM images,

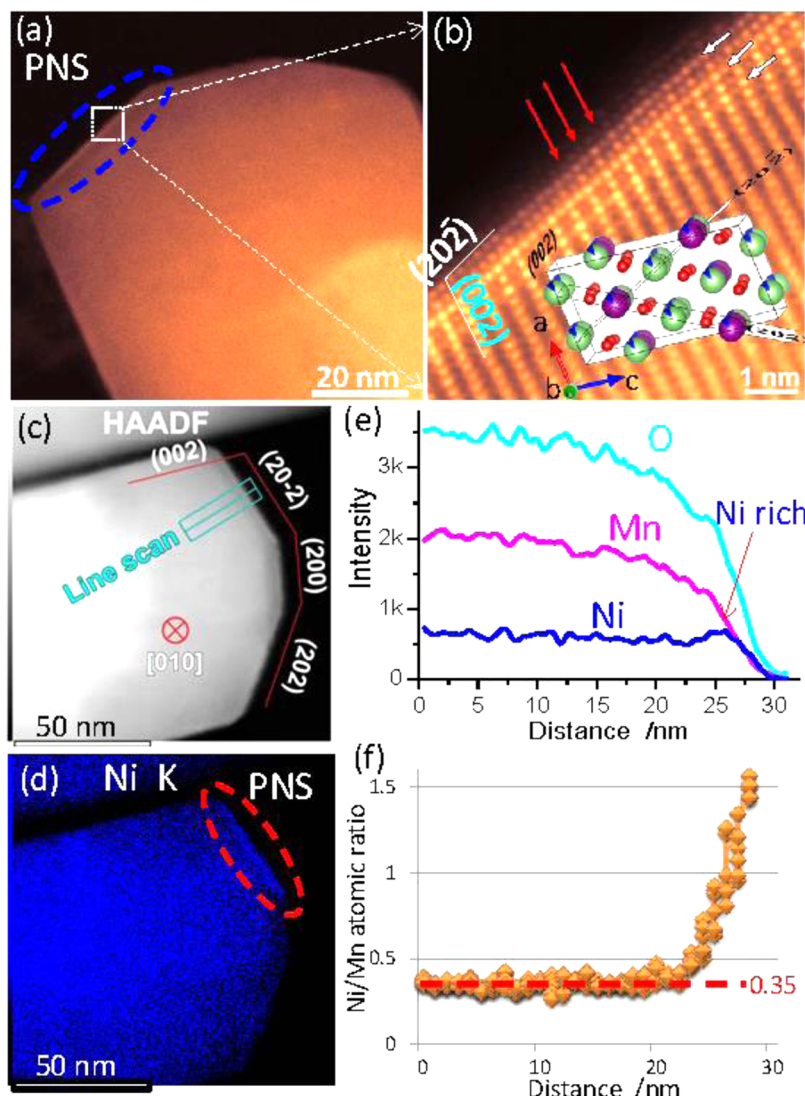


Figure 1. (a) low magnification and (b) high resolution STEM-HAADF images of the PNS layer in a pristine particle. White arrows in (b) indicate ordered features along $(20-2)$ planes. Red arrows in (b) indicated Li-slabs being inserted heavy TM cations in the PNS layer. A $[010]$ direction $C2/m$ crystal structure is shown as inset map in (b). Green: Li; Blue: Ni; Purple: Mn; Red: O. (c) STEM-HAADF image of EDS mapping area. The particle was tilted to $[010]$ zone and its surface facets were determined. (d) Corresponding Ni elemental mapping. (e) Line scan signal counts across the PNS layer, whose location is shown in the STEM-HAADF image; (f) Quantitative Ni/Mn atomic ratios along the line scan. The Ni/Mn ratios are around 0.35 in bulk region, which is close to the designed value 0.33.

the microscope parameters C_c and C_s are 1.2 mm and 0.7 mm, respectively. The STEM-HAADF simulations were conducted by the multislice method implanted in the Kirkland code.^{38,39} For all the structures calculated in this work, the thickness of the supercells is set at 10 nm. The convergence angle and collection angles for the simulation is set in accordance with the experimental values. To incorporate thermal vibrations, four configurations were averaged at 300 K with a probe fwhm 0.6 Å.

Li_2MnO_3 and $\text{LiNi}_{0.5}\text{Mn}_{0.5}\text{O}_2$ are two well-studied cathode materials. The former adopts monoclinic $C2/m$ structure and the latter has an $R\bar{3}m$ layered structure. Because $\text{Li}_{1.2}\text{Ni}_{0.2}\text{Mn}_{0.6}\text{O}_2$ can be expressed as $(50\%\text{Li}_2\text{MnO}_3 + 50\%\text{LiNi}_{0.5}\text{Mn}_{0.5}\text{O}_2)$, there has been a debate on the phase structure of LMR cathode. One is two-phase mixer structure.²⁷ The other is $C2/m$ solid solution structure.^{19,40} For the samples used in this work, high resolution X-ray powder diffraction and intensive TEM observations reveals that the pristine LMR

cathode particles exhibit a $C2/m$ symmetry (see Figure S1 and S2 in the Supporting Information). Compared with ideal $C2/m$ Li_2MnO_3 structure, due to more transition metal (TM) cations being incorporated, disordered TM-planes can be frequently seen in the pristine LMR structure (highlighted in Supporting Information Figure S2d). These disordered planes are due to a local TM segregation in the bulk material. It has been observed that Ni can segregate on particle surface to form a Ni-rich layer,²⁸ which can be called pristine Ni surface layer (PNS). As shown in Figure 1a and b, the current material also shows Ni-rich surface layer as evidenced by the bright contrast under STEM-HAADF imaging. The lattice structure of the Ni rich layer is different from the bulk lattice. Moreover, the surface $(20-2)$ planes show an ordered feature, which is evidenced by their intensity fluctuation as marked by the white arrows in Figure 1b. Based on intensive observations, we found that the PNS layer only formed on the $(20-2)$ surface facets as evidenced by the additional STEM-HAADF images shown in

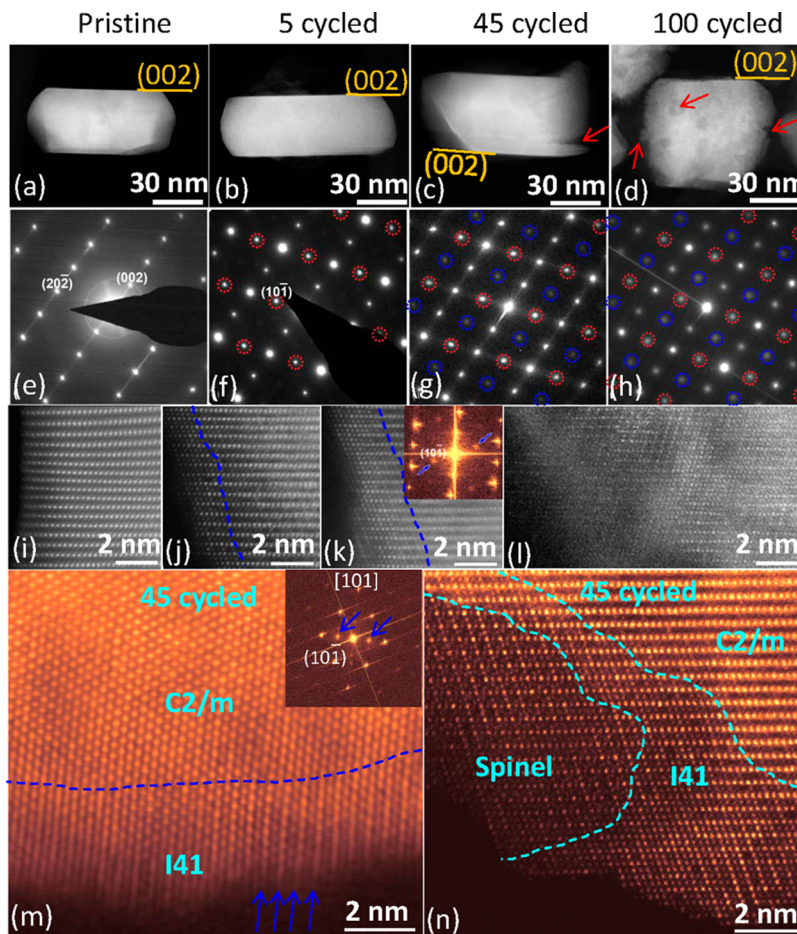


Figure 2. (a-d) Low magnification STEM-HAADF images to show cycling induced corrosion. Cracks and pits are highlighted by red arrows. (002) surface planes show strong resistance to corrosion. e-h) [010] zone axis SAED patterns. Extra diffraction spots appeared in cycled samples, which are highlighted by red and blue circles. Red circles indicated the formation of ordered structure. (10-1) ordered plane is clearly seen after cycling. Blue circles come from double diffraction. (i-l) High resolution STEM-HAADF images to show the cycling induced structure change on particle surfaces. Pristine samples (i) shows homogeneous structure from surface to bulk. Dashed lines in (j, k) highlight the thickness of the SRL. In (l), the whole areas were transformed. (m) [101] zone axis STEM-HAADF image and its fast Fourier transformation image. Blue arrows indicate the ordered features of (20-2) planes and extra diffraction spots. (n) [010] zone axis STEM-HAADF image to show spinel structure and I41 structure in a 45 cycled sample.

Supporting Information Figure S3. Figure 1 (c-f) and Supporting Information Figure S4 show elemental distribution captured by EDS mapping of a pristine particle. In Figure 1c, the particle was tilted to [010] zone axis. As marked in Figure 1(c), five surface facets are well-defined. Elements mapping shows that only the (20-2) facet possesses Ni-segregation (Figure 2d and Supporting Information Figure S4). Detailed line scan results (Figure 1e and f) reveal that Ni is the only enriched element and the Ni/Mn ratio decreases from surface into bulk. The PNS layer has a typical uniform thickness of ~2 nm and can only be observed on (20-2) surface. Since only heavy TM cations (Mn and Ni) are visible in STEM-HAADF images, as indicated by the red arrows in Figure 1b, some TM cations have substituted the Li cation octahedral sites in Li-slabs. Therefore, the composition of PNS is Ni-rich but Li-poor and cannot be ascribed to C2/m symmetry in structure. The structural features of the PNS layer will be discussed in the following section. As the PNS layer has a similar structure with cycling induced surface reconstruction layer (SRL), when observing cycling induced SRLs on cycled particles, (20-2) surface will be avoided.

Cycling induced structural change. In this section, we discuss the structural evolution of the particle upon cyclic charge and discharge. Supporting Information Figure S5 shows the first charge/discharge cycle and capacity as a function of cycle numbers, which shows a proper cell performance. The overall morphological evolution of the particle during the cycling is investigated by STEM-HAADF as shown in Figure 2a-d. It is evident that upon cycling the particle was corroded in the electrolyte, leading to the formation of cracks and pits as shown in Figure 2c and d. Surprisingly, it is found that the corrosion happens only on certain crystallographic facets, typically (200) and (202) planes, which are composed of a mixture of cations and anions (inset of Figure 1(b)). In contrast, the crystallographic planes, such as (002) and (20-2), which are composed of pure cations/anions (inset of Figure 1(b)), are relatively stable and show strong resistance against corrosion. This observation is further confirmed by the conventional TEM images shown in Figure S6 in the Supporting Information. Even though there are some mechanisms to explain how surface corrosion happened,^{23,24} it is still far away from fully understanding its actual process. Obviously, surface corrosion should be closely related to

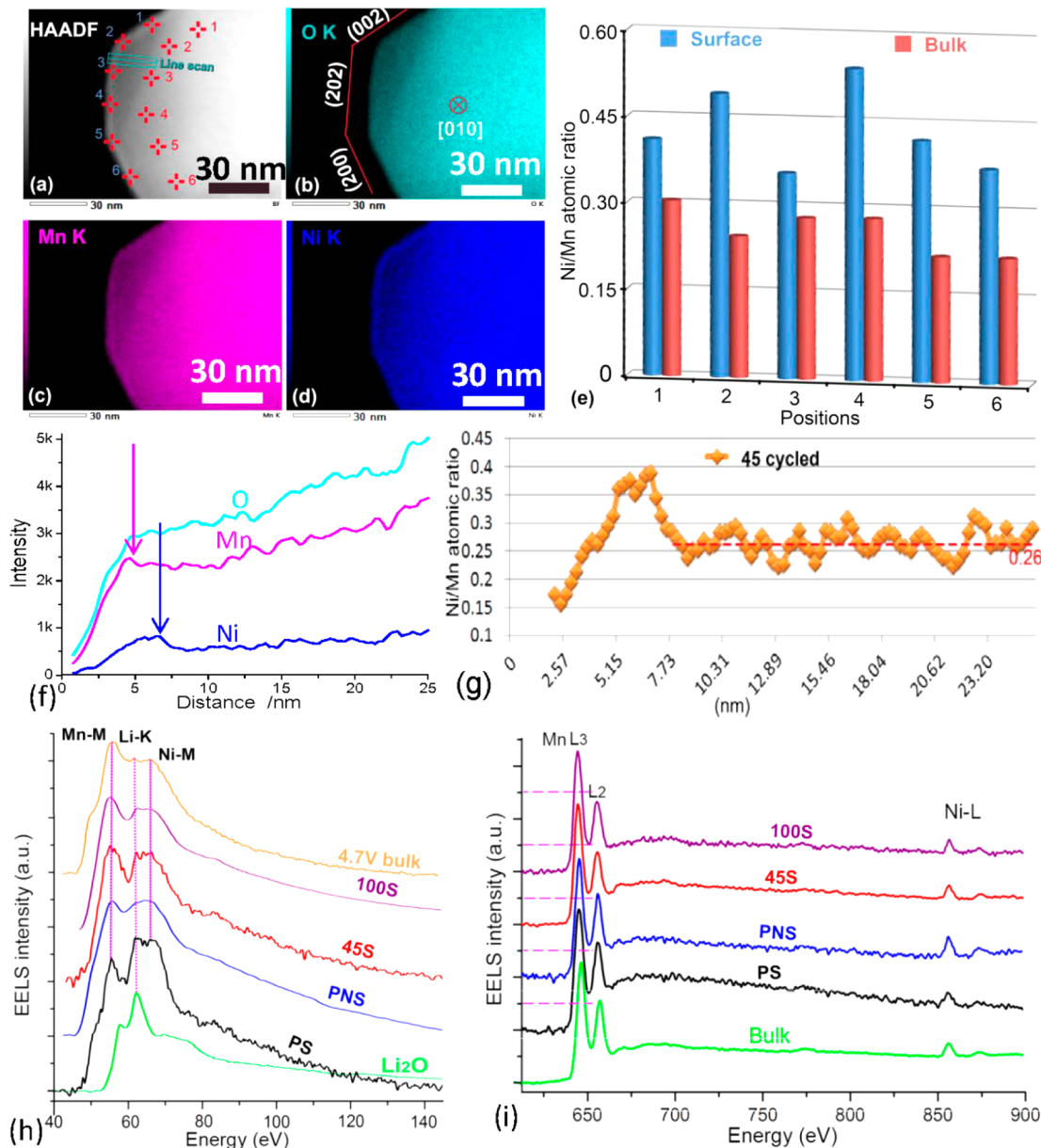


Figure 3. (a-d) EDS mapping results from a 45 cycled LMR particle. The particle was tilted to the [010] zone axis and three surface facets were determined in (b). (e) Quantitative Ni/Mn ratios from surface and bulk positions as marked in (a); (f) line scan signal counts; (g) Quantitative Ni/Mn atomic ratios along the line scan. The Ni/Mn ratios are around 0.26 in bulk region. (h) Low loss EELS spectra and (i) high loss EELS spectra from different samples. 4.7 V bulk: spectrum collected from 4.7 V overcharged sample's bulk region; 100S: spectra collected from the surface of 100 cycled sample; 45S: spectra collected from the surface of 45 cycled sample; PNS: spectra collected from the Ni-rich surface of pristine sample; PS: spectra collected from pristine sample surface without Ni-rich layer; Li₂O: spectrum collected from Li₂O sample; Bulk: spectrum collected from pristine sample's bulk region. The degree of Li-K edge depression is 4.7 V bulk > 100S > 45S ≈ PNS > PS. The order of Mn L₃/L₂ ratio is 100S > 45S > PNS ≈ PS ≈ Bulk.

surface layer's both structural and composition evolution upon cycling.

Upon cycling, the most discernible change of the LMR particle is the formation of a surface reconstruction layer (SRL), as representatively shown by the STEM-HAADF images in Figure 2j-n and HRTEM images in Supporting Information Figure S7. It should be noted that when taking these images, we always avoided the (20-2) surface due to its initial Ni segregation and structure ordering. Structurally, within the SRL, TM cations have occupied the octahedral sites in Li-slabs. The thickness of the SRL increases with increasing number of cycles. Formation of the SRL is also confirmed by

SAED patterns. As shown in Figure 2e-h, compared with pristine sample, cycled samples show extra spots (highlighted by red and blue circles). The blue circles indicate double diffraction spots. The stronger double diffraction spots from 45 and 100 cycled samples indicate they have thicker SRLs. By indexing the SAED patterns, we found the (20-2) planes were ordered and formed by double spacing (10-1) planes, which was further confirmed by high resolution STEM-HAADF images shown in the insets of Figure 2k and 2(m). The blue arrows in Figure 2m indicate the ordering features of (20-2) planes from a [101] zone axis and its corresponding fast Fourier transformation images clearly show extra (10-1) spots

(marked by blue arrows) due to the structural ordering. Thus, the SRL structure is actually an ordered structure, which means extra ordering was introduced during cycling as compared with pristine layered structure. It should be pointed out that the ordered feature is relatively weak and easily damaged during observation under high energy electron beam irradiation. Moreover, as shown in Figure 2n, we also noticed that M_3O_4 type spinel structure was formed at the very outside layer of the SRL after 45 cycles, which indicates that further depletion of the Li happens at the outside of SRL. Usually, the SRL shows a brighter contrast in STEM-HAADF images (Figure 2 and Supporting Information Figure S8), which indicates local enrichment of heavy elements.

Cycling induced chemical composition change. The chemical compositions of the LMR particles after cycling were mapped by using the high efficient EDS spectrometer (Figure 3a-d). In order to compare the structural and chemical composition analysis of the cycled sample with the pristine one, all the samples were tilted to the [010] zone axis (in comparison with Figure 1). Three surface facets, (002), (202) and (200), are in the edge along this orientation as indicated in Figure 3b. Quantitative EDS analysis reveals the following two points. (1) As compared with the pristine one, the SRL of the cycled sample is Ni rich along the (002), (202) and (200) facets as indicated by the Ni intensity map shown in Figure 3d, the EDS point analysis shown in Figure 3e, and the line scan profile shown in Figure 3f. This is further supported by the Mn/Ni ratio as illustrated in Figure 3(g) for which the sample thickness effect is normalized. (2) After cycling, the Ni concentration in the bulk lattice is decreased. This is quantitatively proved by the fact that the Ni/Mn atomic ratio for the 45 cycled sample is about 0.26 (see Figure 3(g)), which is significantly lower than the value of 0.35 for the pristine bulk sample (see Figure 1f). The observation of the formation of Ni rich SRL on the surfaces and depletion of Ni from the bulk lattice conclusively indicates that Ni migrates from the bulk to surface during the cycling of the cathode. This observation is consistent with the DFT calculation results that Ni in the Li slab has a relatively low migration barrier as compared with Li.²⁸ The quantitative EDS line analysis shown in Figure 3f and Supporting Information Figure S9) reveals another intriguing feature: the distribution of Mn and Ni within the thin SRL layer also shows spatial partitions, i.e., Ni-poor structure was observed in the outside edge of the SRL (~2 nm in thickness), while Ni-rich structure was observed in the inner part of the SRL (~6 nm in thickness). This observation probably indicates that Ni in the very outside of the particle is preferentially dissolved into the liquid electrolyte during the cycling. However, this assumption does not conflict with the usually seen higher Mn dissolution into electrolyte, because Ni content is much lower than that of Mn in this LMR cathode. A recent study shows that Ni dissolution can be higher than that of Mn for the Ni-rich cathode.⁴¹ However, it has been noticed that the PNS layer (the (20-2) surface facet) and the SRL on the (002) remain intact during the cycling. Both (20-2) and (002) surface facets are composed of pure cations/anions, while surface facets (200) and (202) are composed of a mixture of cations and anions. Therefore, it can be generally concluded that Ni on the surface with a mixture of cations and anions is prone to dissolve into the electrolyte, but it is not the case for the surface with a pure cations/anions.

Compared with the PNS layer, the cycling induced SRL presents three clear differences. First, the SRL occurred on all

surface, while the PNS layer only formed on the (20-2) surface. Second, the outside edge of the SRL is Ni-poor, while the outside edge of the PNS layer has the highest Ni content. The third difference is that the thickness of SRL shows correlation with cycle numbers and surface facets and varies from particle to particle; while the thickness of PNS layer is almost the same for different particles.

In accordance with the quantitative measurement of the TM elements (Mn and Ni) in the SRL and the PNS layer of both pristine and cycled samples, the Li concentration of these samples was also measured using EELS. The EELS measurement indicates that Li content in the SRL gradually decreases, and eventually depleted with extended cycling. As shown in Figure 3h, the low loss EELS spectra region contained Mn-M edge, Li-K edge and Ni-M edge. In the sample charged to 4.7 V, most of the Li ions have been extracted, which leads to a depressed Li-peak in bulk region. In contrast, as the pristine sample contains a high concentration of Li, the EELS captured on the surface (away from PNS) of the pristine samples (PS) shows a pronounced Li-peak. The EELS spectra obtained from the PNS layer of the pristine sample and the cycled samples (45 cycles (45S) and 100 cycles (100S)) still exhibit moderate Li-peaks, indicating that the Li content in PNS is lower than that of the PS but higher than the samples charged to 4.7 V. Compared with the sample 45S, the sample 100S shows a lower Li-peak. In the core loss region (Figure 3(i)), it is noticed that both the ratio of Mn L_3/L_2 and the energy lost position of Mn depends on the cycle number. According to a two-step method,^{42,43} the valence of the Mn was measured based on the Mn L_3/L_2 ratios. The average valence of Mn cations is reduced to less than 3+ in the SRL, which can introduce large strain due to the Jahn-Teller effect and leads to structural destabilization.⁴⁴ Moreover, reduced Mn cations could gain higher mobility and leads to structural change. After cycling, a shift of the prepeak of O K-edge was noted (Supporting Information Figure S10), which can be attributed to the surface structure transformation.⁴⁵

Structure modeling of the SRL. In the literature, the structure of the SRL has been assigned to rock salt,^{5,20,35} disordered rock salt² and spinel (including disordered-spinel/spinel-like).^{10,21,23} However, as shown in Figure 2, the SRL in LMR cathode actually exhibits an ordered structure, which rules out the rock salt and disordered rock salt structures. For the spinel structure, it can be two kinds of spinel phases: LiM_2O_4 spinel and M_3O_4 spinel. The EELS indicates existence of Li in the SRL. Thus, the LiM_2O_4 spinel is only discussed at this section. The M_3O_4 type spinel will be discussed in next section. Even though the experimental diffraction patterns match with the LiM_2O_4 -spinel, both HRTEM and high resolution STEM-HAADF images (Figures 2) do not match LiM_2O_4 -spinel, because it is evident that all the octahedral site columns were occupied by TM cations. Therefore, the SRL is more likely to be another structure. Thackeray et al. found that when Li was chemically inserted into Mn_3O_4 ,⁴⁶ $LiMn_3O_4$ will be formed with a space group I41 (the ICSD No. is 164994). Based on structure simulation, the SRL observed in the present work is indeed correspondence to the I41 structure. Combining the EDS and EELS analysis, it is estimated that the composition of the SRL is close to LiM_2O_3 ($M=Mn$ and Ni). This conclusion is supported by the comparing the experimental HRTEM and STEM-HAADF images with that of the calculated structure of rock salt, disordered rock salt, spinel and I41 as shown in Figure 4. Evidentially, the tetragonal I41 structure is the best one

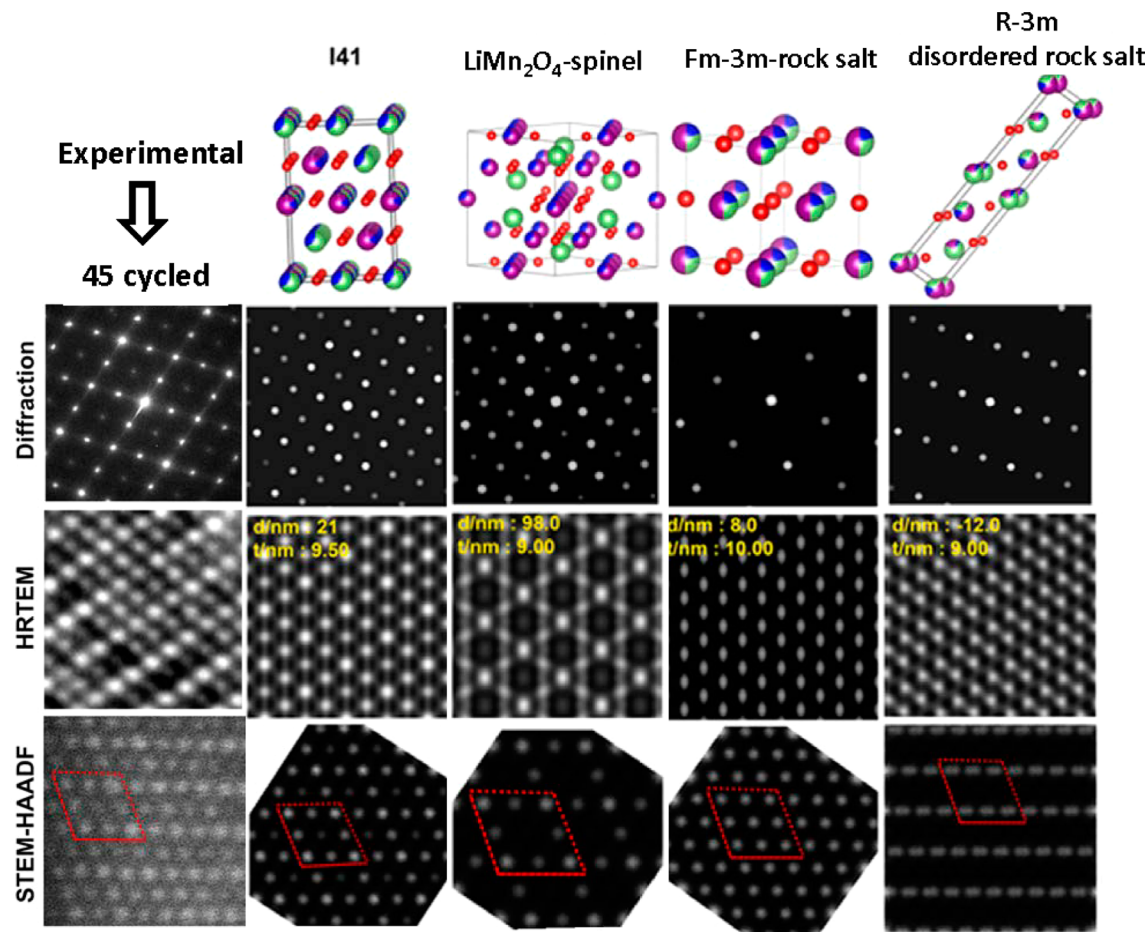


Figure 4. Comparison between experimental results and simulation results of different crystal models for the SRL from the [010] zone axis. I41 structure matches best in the four crystal models.

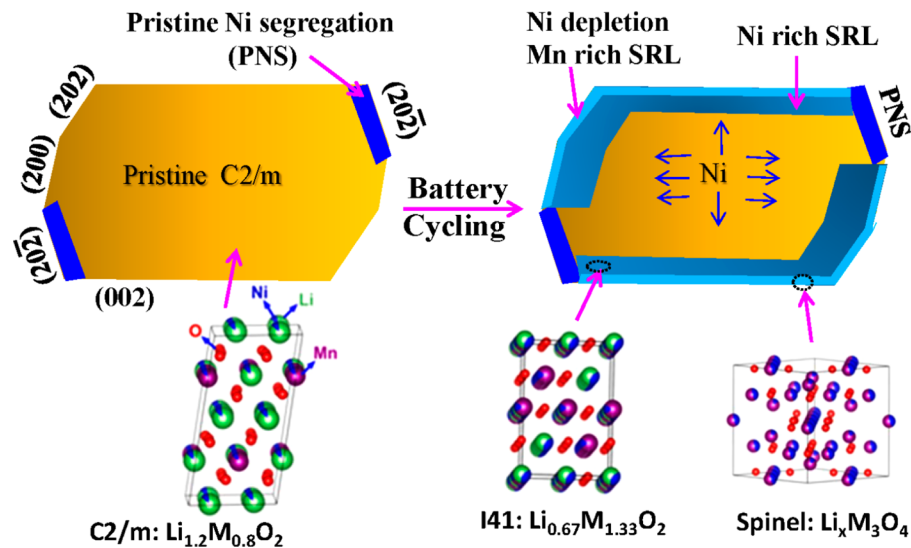


Figure 5. Schematic diagram to show cycling induced surface layer evolution. At left side, the pristine particle has a C2/m structure and PNS layers are located at (20–2) surface planes. After cycling, due to Ni²⁺ migration from bulk to surface, Mn²⁺ surface aggregation and Li⁺ depletion in surface layer, SRL is developed on particle surface except the PNS. The structure of surface layer transforms from original C2/m into I41 and finally developed spinel structure due to progressive TM enrichment and Li depletion. I41 structure is the main phase in the SRL.

matching with experimental results. In Supporting Information Figure S11, we also compare the pristine and cycled samples (100s) from [100] zone axis, which also indicates the SRL has an I41 structure. It should be pointed out that the composition

varies across the SRL from outer surface to inner layer, therefore, an average composition value was chosen to define the SRL composition.

Above experimental observation is also consistently supported by the density functional theory (DFT) calculation of the lattice energy, which indicates that the I41 has the lowest lattice energy. In order to understand the relative stability of rock salt, disordered rock salt and I41 crystal models, we calculated the lattice energy of each phase using the Vienna ab initio simulation package within the framework of DFT.⁴⁷ The three structures contain the same Li:Ni:Mn:O proportion, i.e. 0.67:0.43:0.9:2. Our calculations show that lattice energy of I41 structure is about 0.10 eV lower than that of disordered rock salt structure and 0.11 eV lower than that of rock salt structure for the $\text{Li}_{0.67}\text{Mn}_{0.9}\text{Ni}_{0.43}\text{O}_2$ molecule. Hence, I41 phase is more stable than the rock salt and disordered rock salt at the composition of $\text{Li}_{0.67}\text{Ni}_{0.43}\text{Mn}_{0.9}\text{O}_2$.

Depending on the Li, TM and O composition, different phases can be formed. For example, Li_2MnO_3 adopts a monoclinic $C2/m$ structure; LiMnO_2 and $\text{Li}(\text{Ni}_{0.5}\text{Mn}_{0.5})\text{O}_2$ adopt the trigonal $R\bar{3}m$ structure; LiMn_2O_4 adopts a cubic $Fd\bar{3}m$ spinel structure, which could become Mn_3O_4 spinel with the complete depletion of Li. Thus, Li-M-O material should have a most stable structure with a given composition. As convinced by our EDS and EELS analysis, the cycling induced SRL is a TM-rich and Li-poor structure, which indicates the formation of SRL involves a progressive enrichment of TM and Li depletion upon cycling. In many cases, composition change of a material will trigger structural transformation. Therefore, we believe the structure change of the SRL is driven by its composition change. As shown in Figure 2n, we noticed a Li-depletion M_3O_4 -spinel was developed outside of the I41 structure, which indicates the I41 structure can finally transformed into M_3O_4 -spinel with further depletion of Li content. Thus, a phase transformation sequence for the surface layer is proposed as $C2/m \rightarrow \text{I41} \rightarrow \text{M}_3\text{O}_4$ -spinel. This conclusion is also supported by Figure 2l which shows the outer layer of cycled sample (100S) exhibits more clear spinel-featured structure.

Overall, upon continuous cycling of the battery, a progressive TM enrichment and Li depletion process is undergoing at the surface of LMR particles, leading to the formation of SRL. Structurally, in accordance with the chemical composition change, the SRL went to a phase transition sequences of $C2/m \rightarrow \text{I41} \rightarrow \text{M}_3\text{O}_4$ -spinel. In Figure 5, we schematically show the surface layer evolution process upon continuous cycling. At left side, it shows a pristine $C2/m$ phase LMR particle with PNS layers on (20–2) planes. After cycling, thin SRL is developed on particle surface except the PNS layers, which is due to Ni migration from bulk to surface and Mn²⁺ cation surface aggregation. In the SRL, the very outside layer eventually become Mn-rich and Ni-depleted and the inner layer is Ni-rich. Because of the TM segregation and Li-depletion in the SRL, the original $C2/m$ phase loses its layered structure and transformed into I41 structure and further cycling finally transformed outside layer into M_3O_4 -spinel.

It has been generally accepted that the voltage fading and capacity decaying are in some degrees directly correlated with the formation of the SRL on the particle. On the other hand, it is also speculated that related to such a thin nature of SRL, the SRL may not be the dominating factor for the observed voltage fading and capacity decaying of LMR cathode. The present observation of the structural features and chemical composition evolution of the SRL upon cycling and its direct correlation with the compositional change of the bulk lattice firmly indicate that the voltage fading and capacity decaying of LMR cathode is

indeed correlated to the SRL on the surface of each particle. This conclusion is supported by the following points. (1) Gradual migration of Ni from bulk lattice to the surface will lead to gradual depletion of Ni from the bulk lattice and directly leads to capacity fading. Furthermore, with a decreasing Ni content, the Mn–Ni interaction becomes weaker which will result in material destabilization.¹³ (2) Dissolution of the cations, especially Ni along crystal facets that are terminated with a mixture of both cation and anion, leads to corrosion of cathode particle and consequently the capacity fading. Chen et al have demonstrated that for spinel $\text{LiMn}_{1.5}\text{Ni}_{0.5}\text{O}_4$ cathode materials, particle morphology has a dominant effect on spinel transport properties, indicating the great role of surface structure on the stability of the particle in liquid.⁴⁸ (3) The SRL is a TM rich layer by which the Li position in the Li slab was gradually occupied by the TM caions following a certain diffusion path, which has been discussed in details based on theoretical calculations.^{1,18,32} According to a recent simulation by Ceder et al.,² the SRL will results in increasing barrier for Li migration, therefore contributing to the voltage fade. (4) The formation of patches of Li depleted spinel at the very surface of the particle essentially cut off the Li transport path, making the Li in the particle not accessible and therefore leading to both voltage and capacity fading. (5) The observation of the high stability of pure cation terminated facets typically such as (002) and (20–2) in the electrolyte appears to be rather intriguing for designing particle against corrosion if these type of surfaces are enlarged. However, these surfaces will probably block the Li transport path. Therefore, the contradictory role of this type of surfaces in the particle need to be optimized.

In summary, pristine and cycled LMR cathode materials were investigated by advanced microscopes. For the pristine LMR particles, Ni-segregation surface layer are always found at (20–2) facets. After cycling, LMR particle developed a surface reconstruction layer (SRL) with increased thickness upon cycling. Detailed structure imaging and electron diffraction confirmed the SRL formed an ordered structure. Spectroscopy analysis reveals that the SRL is TM-rich and Li-poor phase which is due to Ni migration from bulk to surface and Mn surface aggregation. The structure of the SRL is determined to be a tetragonal structure with space group of I41/amd which then transforms into a M_3O_4 -spinel structure with minimal Li-content. Thus, a sequential structure transformation of $C2/m \rightarrow \text{I41} \rightarrow \text{M}_3\text{O}_4$ -Spinel occurs on particle surface upon cycling, which is due to a progressive TM enrichment and Li depletion. The formation of the SRL on LMR particle surface is believed to be the main reason for the voltage fade, poor rate capability and capacity decay of LMR materials. These findings on composition change, structural evolution of the surface layer on LMR as well as their effects on materials' electrochemical properties provide valuable understanding for the material structure and its fading mechanism. They demonstrate that it is crucial to further optimize the surface of LMR to obtain a cathode material with both high capacity and voltage stability.

■ ASSOCIATED CONTENT

S Supporting Information

Additional XRD pattern, electrochemical data, TEM images and figures are supplied in the Supporting Information. This material is available free of charge via the Internet at <http://pubs.acs.org>.

AUTHOR INFORMATION

Corresponding Authors

*E-mail: Jiguang.zhang@pnnl.gov.
*E-mail: Chongmin.wang@pnnl.gov.

Notes

The authors declare no competing financial interest.

ACKNOWLEDGMENTS

We appreciate the beneficial discussion of Dr. Ping Lu of Sandia National Laboratory during the course of this work. This work was supported by the Assistant Secretary for Energy Efficiency and Renewable Energy, Office of Vehicle Technologies of the U.S. Department of Energy under Contract No. DE-AC02-05CH11231, Subcontract No. 6951379 under the Batteries for Advanced Transportation Technologies (BATT) Program. The high spatial resolution and high efficiency EDS analysis described in this paper is supported by the Laboratory Directed Research and Development Program as part of the Chemical Imaging Initiative at Pacific Northwest National Laboratory (PNNL). The work was conducted in the William R. Wiley Environmental Molecular Sciences Laboratory (EMSL), a national scientific user facility sponsored by DOE's Office of Biological and Environmental Research and located at PNNL. PNNL is operated by Battelle for the Department of Energy under Contract DE-AC05-76RLO1830. The Materials synthesis was carried out at Argonne National Laboratory, which is operated for the U.S. Department of Energy by University of Chicago Argonne, LLC, under contract DE-AC0Z-06CH11357.

REFERENCES

- (1) Kang, K. S.; Meng, Y. S.; Breger, J.; Grey, C. P.; Ceder, G. *Science* **2006**, *311*, 977–980.
- (2) Lee, J.; Urban, A.; Li, X.; Su, D.; Hautier, G.; Ceder, G. *Science* **2014**, *343*, 519–22.
- (3) Meng, Y. S.; Arroyo-de Dompablo, M. E. *Acc. Chem. Res.* **2013**, *46*, 1171–1180.
- (4) Xu, J.; Lee, D. H.; Meng, Y. S. *Funct. Mater. Lett.* **2013**, *6*, 1330001.
- (5) Nam, K. W.; Bak, S. M.; Hu, E. Y.; Yu, X. Q.; Zhou, Y. N.; Wang, X. J.; Wu, L. J.; Zhu, Y. M.; Chung, K. Y.; Yang, X. Q. *Adv. Funct. Mater.* **2013**, *23*, 1047–1063.
- (6) Sun, Y. K.; Myung, S. T.; Park, B. C.; Prakash, J.; Belharouak, I.; Amine, K. *Nat. Mater.* **2009**, *8*, 320–4.
- (7) Ceder, G.; Chiang, Y. M.; Sadoway, D. R.; Aydinol, M. K.; Jang, Y. I.; Huang, B. *Nature* **1998**, *392*, 694–696.
- (8) Tarascon, J. M.; Armand, M. *Nature* **2001**, *414*, 359–67.
- (9) Marom, R.; Amalraj, S. F.; Leifer, N.; Jacob, D.; Aurbach, D. *J. Mater. Chem.* **2011**, *21*, 9938–9954.
- (10) Thackeray, M. M.; Johnson, C. S.; Vaughey, J. T.; Li, N.; Hackney, S. A. *J. Mater. Chem.* **2005**, *15*, 2257–2267.
- (11) Zheng, J.; Gu, M.; Genc, A.; Xiao, J.; Xu, P.; Chen, X.; Zhu, Z.; Zhao, W.; Pullan, L.; Wang, C.; Zhang, J. G. *Nano Lett.* **2014**, *14*, 2628–35.
- (12) Kam, K. C.; Mehta, A.; Heron, J. T.; Doeff, M. M. *J. Electrochem. Soc.* **2012**, *159*, A1383–A1392.
- (13) Kim, D.; Croy, J. R.; Thackeray, M. M. *Electrochem. Commun.* **2013**, *36*, 103–106.
- (14) Guan, D.; Jeevarajan, J. A.; Wang, Y. *Nanoscales* **2011**, *3*, 1465–1469.
- (15) Lu, Z. H.; MacNeil, D. D.; Dahn, J. R. *Electrochem. Solid St.* **2001**, *4*, A191–A194.
- (16) Wang, Y.; Cao, G. Z. *Adv. Mater.* **2008**, *20*, 2251–2269.
- (17) Meng, Y. S.; Ceder, G.; Grey, C. P.; Yoon, W. S.; Jiang, M.; Bréger, J.; Shao-Horn, Y. *Chem. Mater.* **2005**, *17*, 2386–2394.
- (18) Li, H. H.; Yabuuchi, N.; Meng, Y. S.; Kumar, S.; Breger, J.; Grey, C. P.; Shao-Horn, Y. *Chem. Mater.* **2007**, *19*, 2551–2565.
- (19) Jarvis, K. A.; Deng, Z. Q.; Allard, L. F.; Manthiram, A.; Ferreira, P. J. *Chem. Mater.* **2011**, *23*, 3614–3621.
- (20) Lin, F.; Markus, I. M.; Nordlund, D.; Weng, T. C.; Asta, M. D.; Xin, H. L.; Doeff, M. M. *Nat. Commun.* **2014**, *5*, 3529.
- (21) Boulineau, A.; Simonin, L.; Colin, J. F.; Bourbon, C.; Patoux, S. *Nano Lett.* **2013**, *13*, 3857–63.
- (22) Xu, B.; Fell, C. R.; Chi, M. F.; Meng, Y. S. *Energy Environ. Sci.* **2011**, *4*, 2223–2233.
- (23) Gu, M.; Belharouak, I.; Zheng, J. M.; Wu, H. M.; Xiao, J.; Genc, A.; Amine, K.; Thevuthasan, S.; Baer, D. R.; Zhang, J. G.; Browning, N. D.; Liu, J.; Wang, C. M. *ACS Nano* **2013**, *7*, 760–767.
- (24) Zheng, J.; Gu, M.; Xiao, J.; Zuo, P.; Wang, C.; Zhang, J. G. *Nano Lett.* **2013**, *13*, 3824–30.
- (25) Qian, D.; Xu, B.; Chi, M.; Meng, Y. S. *Phys. Chem. Chem. Phys.* **2014**, *16*, 14665–14668.
- (26) Fell, C. R.; Qian, D. N.; Carroll, K. J.; Chi, M. F.; Jones, J. L.; Meng, Y. S. *Chem. Mater.* **2013**, *25*, 1621–1629.
- (27) Yu, H.; Ishikawa, R.; So, Y. G.; Shibata, N.; Kudo, T.; Zhou, H.; Ikuhara, Y. *Angew. Chem., Int. Ed. Engl.* **2013**, *52*, 5969–73.
- (28) Gu, M.; Belharouak, I.; Genc, A.; Wang, Z.; Wang, D.; Amine, K.; Gao, F.; Zhou, G.; Thevuthasan, S.; Baer, D. R.; Zhang, J. G.; Browning, N. D.; Liu, J.; Wang, C. *Nano Lett.* **2012**, *12*, 5186–91.
- (29) Rana, J.; Stan, M.; Kloepsch, R.; Li, J.; Schumacher, G.; Welter, E.; Zizak, I.; Banhart, J.; Winter, M. *Adv. Energy Mater.* **2014**, *4*, 1300998.
- (30) Li, B.; Gu, M.; Nie, Z. M.; Shao, Y. Y.; Luo, Q. T.; Wei, X. L.; Li, X. L.; Xiao, J.; Wang, C. M.; Sprenkle, V.; Wang, W. *Nano Lett.* **2013**, *13*, 1330–1335.
- (31) Yabuuchi, N.; Yoshii, K.; Myung, S. T.; Nakai, I.; Komaba, S. *J. Am. Chem. Soc.* **2011**, *133*, 4404–4419.
- (32) Breger, J.; Meng, Y. S.; Hinuma, Y.; Kumar, S.; Kang, K.; Shao-Horn, Y.; Ceder, G.; Grey, C. P. *Chem. Mater.* **2006**, *18*, 4768–4781.
- (33) Armstrong, A. R.; Holzapfel, M.; Novak, P.; Johnson, C. S.; Kang, S. H.; Thackeray, M. M.; Bruce, P. G. *J. Am. Chem. Soc.* **2006**, *128*, 8694–8698.
- (34) Qian, D.; Xu, B.; Chi, M.; Meng, Y. S. *Phys. Chem. Chem. Phys.* **2014**, *16*, 14665–8.
- (35) Guilmard, M.; Croguennec, L.; Denoux, D.; Delmas, C. *Chem. Mater.* **2003**, *15*, 4476–4483.
- (36) Gu, M.; Genc, A.; Belharouak, I.; Wang, D. P.; Amine, K.; Thevuthasan, S.; Baer, D. R.; Zhang, J. G.; Browning, N. D.; Liu, J.; Wang, C. M. *Chem. Mater.* **2013**, *25*, 2319–2326.
- (37) Zhang, X. F.; Xu, R.; Li, L.; Yu, C.; Ren, Y.; Belharouak, I. *J. Electrochem. Soc.* **2013**, *160*, A1079–A1083.
- (38) Hillyard, S.; Silcox, J. *Ultramicroscopy* **1995**, *58*, 6–17.
- (39) Kirkland, E. J.; Loane, R. F.; Silcox, J. *Ultramicroscopy* **1987**, *23*, 77–96.
- (40) Lu, Z. H.; Beaulieu, L. Y.; Donaberger, R. A.; Thomas, C. L.; Dahn, J. R. *J. Electrochem. Soc.* **2002**, *149*, A778–A791.
- (41) Noh, H.-J.; Myung, S.-T.; Lee, Y. J.; Sun, Y.-K. *Chem. Mater.* **2014**, *26*, 5973–5979.
- (42) Pearson, D. H.; Ahn, C. C.; Fultz, B. *Phys. Rev. B* **1993**, *47*, 8471–8478.
- (43) Wang, Z. L.; Yin, J. S.; Jiang, Y. D. *Micron* **2000**, *31*, 571–80.
- (44) Ohzuku, T.; Kitagawa, M.; Hirai, T. *J. Electrochem. Soc.* **1990**, *137*, 769–775.
- (45) Hwang, S.; Chang, W.; Kim, S. M.; Su, D.; Kim, D. H.; Lee, J. Y.; Chung, K. Y.; Stach, E. A. *Chem. Mater.* **2014**, *26*, 1084–1092.
- (46) Thackeray, M. M.; David, W. I. F.; Bruce, P. G.; Goodenough, J. B. *Mater. Res. Bull.* **1983**, *18*, 461–472.
- (47) Kresse, G.; Hafner, J. *Phys. Rev. B* **1993**, *47*, 558–561.
- (48) Hai, B.; Shukla, A. K.; Duncan, H.; Chen, G. Y. *J. Mater. Chem. A* **2013**, *1*, 759–769.